Harmonization of technical image quality in computed tomography: comparison between different reconstruction algorithms and kernels from six scanners

Mikael A.K. Juntunen[a,b*], Jari Rautiainen[a,c], Nina E. Hänninen[d], Antti O. Kotiaho[a,e]

[a]Department of Diagnostic Radiology, Oulu University Hospital, Oulu, Finland

[b]Research Unit of Medical Imaging, Physics and Technology, University of Oulu, Oulu, Finland

[c]Department of Radiology, Lapland Central Hospital, Rovaniemi, Finland

[d]Department of Applied Physics, University of Eastern Finland, Kuopio, Finland

[e]Suomen Terveystalo Oy, Oulu, Finland

*Corresponding author. Contact information: Electronic mail: mikael.juntunen@ppshp.fi, Address: Oulu University Hospital, POB 50, FI-90029, OYS, Finland.

ABSTRACT

Purpose: The radiology department faces a large number of reconstruction algorithms and kernels during their computed tomography (CT) optimization process. These reconstruction methods are proprietary and ensuring consistent image quality between scanners is becoming increasingly difficult. This study contributes to solving this challenge in CT image quality harmonization by modifying and evaluating a reconstruction algorithm and kernel matching scheme.

Methods: The Catphan 600 phantom was scanned with six different CT scanners from four vendors. The phantom was scanned with volumetric CT dose indices (CTDIvols) of 10 mGy and 40 mGy, and the data were reconstructed using 1 mm and 5 mm slices with each combination of reconstruction algorithm, body region kernel, and iterative and deep learning reconstruction strength.

A matching scheme developed in previous research, which utilizes the noise power spectrum (NPS) and modulation transfer function (MTF), was modified based on our organization's needs and used to identify the matching reconstruction algorithms and kernels between different scanners.

Results: The matching paradigm produced good matching results, and the mean ± standard deviation (median) matching function values for the different acquisition settings were (a value of 1 indicates a perfect match): CTDIvol 10 mGy, 1 mm slice: 0.78 ± 0.31 (0.94); CTDIvol 10 mGy, 5 mm slice: 0.75 ± 0.33 (0.93); CTDIvol 40 mGy, 1 mm slice: 0.81 ± 0.28 (0.95); CTDIvol 40 mGy, 5 mm slice: 0.75 ± 0.33 (0.93). In general, soft reconstruction kernels, *i.e.,* noise-reducing kernels that reduce sharpness, of one vendor were matched with the soft kernels of another vendor, and vice versa for sharper kernels.

Conclusions: Combined quantitative assessment of NPS and MTF allows effective strategy for harmonization of technical image quality between different CT scanners. A software was also shared to support CT image quality harmonization in other institutions.

Keywords: Computed tomography, image quality, modulation transfer function, noise power spectrum, reconstruction

1. INTRODUCTION

Computed tomography (CT) has advanced significantly, both in terms of imaging hardware and novel reconstruction algorithms. Therefore, the radiology departments face various options to optimize the scanning protocols. Notably, the advances in computation algorithms have introduced various proprietary reconstruction methods and kernels that are typically distinguished into soft-tissue, lung, and bone kernels. Consequently, ensuring consistent imaging quality between different CT scanners, scanner generations, and vendors is becoming increasingly challenging. This harmonization is often implemented using the noise magnitude, characterized as the standard deviation of Hounsfield Units (HUs) in a homogeneous region-of-interest, and the volumetric CT dose index (CTDIvol). Although this approach is a good preliminary approach for adapting the dose and noise between different scanners, it does not consider the differences in noise texture and spatial resolution – both necessary measures that also influence the subjective image quality. Furthermore, for iterative reconstruction (IR) methods, noise magnitude and spatial resolution may exhibit a non-linear relationship (Richard *et al* 2012), and adapting image noise magnitude, contrast-to-noise ratio (CNR), and resolution may become difficult with these methods (see Appendix B and C of the supplementary document).

Noise texture defines the intensity correlation of neighboring pixels. More intuitively, it determines the coarseness of noise. In practice, the noise power spectrum (NPS) is used to determine the noise texture of an image (Boedeker *et al* 2007, Boedeker and McNitt-Gray 2007). The NPS quantifies the noise power as a function of the spatial frequency, offering information about the magnitude and the frequency distribution of noise (Verdun *et al* 2015). The spatial resolution is another critical measure of a CT scanner and imaging protocol since it determines the size of the smallest detectable object (Verdun *et al* 2015). The modulation transfer function (MTF) is commonly utilized to evaluate the resolution of the protocol, which specifies the transfer of spatial frequencies through a CT system.

NPS has been utilized to match the noise texture between two scanners from different vendors using the American College of Radiology CT accreditation phantom (Solomon *et al* 2012). With an attempt to also involve the spatial resolution in the assessment of technical image quality, Winslow et al presented a technique that includes the MTF, NPS, and CTDIvol in the matching process (Winslow *et al* 2017). This matching paradigm allowed direct mapping of CT kernels between two different scanners, yielding consistent technical image quality.

The purpose of this study was to further modify and evaluate the aforementioned matching technique by Winslow et al (Winslow *et al* 2017) for the CT scanners and reconstruction techniques found in our local hospital district. More

specifically, the performance of a modified version of this technique was assessed for six different scanners from four vendors. In addition, a graphical user interface tool is provided for our peers for conducting image quality harmonization in their radiology departments. Furthermore, the performance of two alternative image quality harmonization approaches, CNR- and structural similarity index-based techniques, are addressed in Appendix C.

2. MATERIALS AND METHODS

2.1. Phantoms, scanners and measurement parameters

The Catphan 600 phantom (The Phantom Laboratory, NY, US) was measured with six different CT scanners. The necessary information on the utilized scanners and the respective imaging parameters are summarized in Table I. Two separate acquisitions were performed, with CTDIvol values of 10 mGy and 40 mGy, as was carried out by Winslow et al (Winslow *et al* 2017). Slices with thicknesses of 5 mm and 1 mm were reconstructed with 1 mm increments. GE scanners did not allow for 1 mm increments/slice thickness, and therefore, 1.25 mm was utilized. Excluding the head kernels, each available kernel was reconstructed with each plausible reconstruction algorithm, *i.e.,* filtered back projection (FBP), IR, and deep learning image reconstruction (DLIR). Furthermore, each available

Table I. CT scanners, scanning parameters, and reconstruction parameters.

Setting	Siemens SOMATOM Definition Flash	Siemens SOMATOM Drive	Toshiba Aquilion One Vision Edition	Philips Ingenuity CT	GE Discovery 690	GE Revolution CT
kVp	120	120	120	120	120	120
CTDIvol (mGy)	10.0/40.0	10.0/40.0	9.6/39.6	10.1/39.9	10.1/40.0	10.0/40.0
Pitch factor	1.0	1.0	0.95	1.0	0.984	0.992
Rotation time (s)	1.0	1.0	1.0	1.0	1.0	1.0
DFOV (mm)	205	205	205	205	205	205
Reconstruction size	512 × 512	512 × 512	512 × 512	512 × 512	512 × 512	512 × 512
Collimation (mm)	0.6 × 64	0.6 × 64	0.5 × 80	0.625 × 64	0.625 × 64	0.625 × 64
Slice thickness (mm)	1.0/5.0	1.0/5.0	1.0/5.0	1.0/5.0	1.25/5.0	1.25/5.0
Reconstruction algorithm	FBP, SAFIRE[1]	FBP, ADMIRE[2]	FBP, AIDR 3D[3]	FBP, iDose[4], IMR[5]	FBP, ASIR[6]	FBP, ASIR-V[7], TrueFidelity[8]

[1]Sinogram-affirmed iterative reconstruction, [2]Advanced modeleled iterative reconstruction, [3]Adaptive Iterative Dose Reduction, [4]Fourth-generation hybrid iterative reconstruction, [5]Iterative model reconstruction, [6]Adaptive statistical iterative reconstruction, [7]New generation adaptive statistical iterative reconstruction, [8]Deep learning image reconstruction (Standard kernel only).

IR and DLIR strength was reconstructed. These different reconstruction algorithms are briefly described in section 2.2.

The information regarding the reconstruction algorithm, kernel, and IR strength is abbreviated following the syntax used by the manufacturers. For the Siemens scanners, the abbreviation: I30s\3 for SOMATOM Definition Flash indicates that the I30s kernel was used with SAFIRE strength of 3. For Toshiba, the syntax FC43 (AIDR 3D STD) means the FC43 kernel with standard AIDR 3D strength. With Philips, the abbreviation iDose (4)/B means that the iDose reconstruction algorithm was utilized with an IR strength of 4 and the B-kernel. Finally, as an illustration for the GE scanners, the abbreviation STD_AR90 for the Revolution CT indicates a standard kernel with 90% ASIR-V strength.

2.2. Overview of the reconstruction algorithms

The sinogram affirmed iterative reconstruction (SAFIRE) (Siemens Healthcare, Forchheim, Germany) is an IR method that utilizes weighted FBP reconstruction as its initial reconstruction estimate. Using this initial estimate, it performs two subsequent iteration loops – the first in the projection and the second in the reconstruction domain. Noise is reduced in both domains during each iteration. (Grant and Raupach 2012)

The advanced modeled iterative reconstruction (ADMIRE) (Siemens Healthcare, Forchheim, Germany) is a model-based IR algorithm that incorporates a model for photon counting statistics to reduce image noise and models the imaging geometry during the forward projection. As a model-based method, ADMIRE performs forward and back projection during each iteration of the algorithm. (Ramirez-Giraldo *et al* 2014)

Third-generation adaptive iterative dose reduction (AIDR 3D; Canon Medical Systems, Otawara, Japan) is an IR algorithm that, similarly to SAFIRE, incorporates two subsequent iteration loops for projection and reconstruction domains. The algorithm includes a reduction for photon starvation, electronic and statistical noise in the projection domain, and a quantum noise reduction in the reconstruction domain. Furthermore, a scanner model is utilized during the noise reduction in the projection domain. AIDR 3D Enhanced extends on the traditional AIDR 3D by including an NPS model, aiming to produce finer noise texture, and optimizing the FBP blending ratio and the number of iterations. (Angel 2012, Hernandez-Giron *et al* 2018)

iDose[4] (Philips Healthcare, Best, the Netherlands) performs noise reduction iteratively while aiming to preserve the edges. Separate iteration loops are utilized, first in the projection and subsequently in the image domain (Hou *et al* 2012).

IMR (Philips Healthcare, Best, the Netherlands) is a model-based iterative reconstruction method (the vendor used the term knowledge-based iterative model reconstruction (Mehta *et al* 2013)). IMR considers noise statistics and system physics (detector sampling, angular sampling, and imaging system geometry) during the reconstruction.

Adaptive statistical iterative reconstruction (ASIR) (GE Healthcare, Waukesha, WI, USA) is a full-statistical IR method that includes a noise model in the projection domain and iteratively denoises the image using forward and back projections during each iteration. The result of the ASIR algorithm is blended with FBP to produce the final reconstruction. (Willemink *et al* 2013)

Compared to traditional model-based IR, ASIR-V (GE Healthcare, Waukesha, WI, USA) has reduced the extent of system optics modeling (X-ray source and detector), allowing reduced computation times. Furthermore, ASIR-V includes models for photon and electronic noise, imaged object, and physics. (Fan *et al* 2014)

TrueFidelity (GE Healthcare, Waukesha, WI, USA) is a DLIR algorithm that utilizes convolutional neural networks (CNNs) to produce the reconstruction. The CNN was trained to map the input data, *i.e.,* projection data from low radiation dose acquisition, into a ground truth FBP reconstruction of the same object with a high radiation dose. (Hsieh *et al* 2019)

2.3. Image quality harmonization process

The NPS and MTF were determined utilizing the Catphan modules CTP 486 and CTP 528, respectively (Figure 1). Consecutive slices of the image uniformity module CTP 486 were subtracted, and these subtracted slices were radially sampled with eight 50x50-pixel regions-of-interest from 31 slices, producing 248 noise realizations. The two-dimensional NPS was determined from these noise realizations, and subsequently, this two-dimensional NPS was radially averaged. The one-dimensional, radial NPS was used for the determination of noise texture. This strategy has been addressed in more depth in a number of publications (Verdun *et al* 2015, Juntunen *et al* 2021), and the reader is referred to these studies for further information. The CTP 528 contains two tungsten carbide beads with

0.28 mm diameter that act as point sources. A slice containing one of these beads was utilized for determining the MTF from the point-spread function.

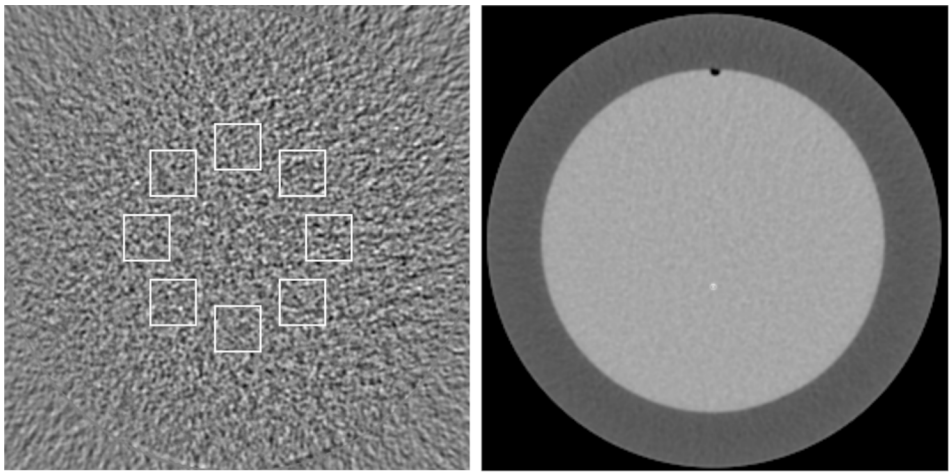

a) ROI sampling for the determination of NPS.

b) Slice for the evaluation of MTF.

Figure 1. a) Determination of noise power spectrum (NPS) from the subtraction image. b) Slice used for the evaluation of the modulation transfer function (MTF).

The matching paradigm largely follows the method described in detail in the previous work by Winslow et al (Winslow *et al* 2017). In summary, the approach utilizes the normalized NPS (nNPS), MTF, and CTDIvol in the matching process. For matching the dose, the relative difference was determined:

$$d_{ij} = \frac{d_j - d_i}{d_i}. \tag{1}$$

with *i* and *j* denoting the target reconstruction and the to-be-matched reconstruction, respectively. The dose parameter (d_i) was the CTDIvol-value of the measurement *i*.

The study by Winslow et al utilized the peak frequency difference between the nNPS curves and the spatial frequency at which the MTF is decreased by 50% to match the noise texture and image resolution. In this study, the root-mean-square error (RMSE) was used for matching the noise texture and resolution:

$$t_{ij} = \frac{\|nNPS_j - nNPS_i\|_2}{\|nNPS_i\|_2}, \tag{2}$$

$$r_{ij} = \frac{\|MTF_j - MTF_i\|_2}{\|MTF_i\|_2}, \tag{3}$$

where *nNPS* and *MTF* are equidistantly sampled in the spatial frequency domain with 0.05 1/mm increments for the target reconstruction and the to-be-matched reconstruction. The matching function value (m-value), m_{ij}, is a weighted product

$$m_{ij} = D(-d_{ij}, a_d, c_d)T(t_{ij}, a_t, c_t)R(r_{ij}, a_r, c_r), \tag{4}$$

where a higher value indicates better agreement between the reconstructions (a value of 1 indicates a perfect match). The matched reconstruction kernel is the one that produces the highest matching function value. *D, T,* and *R* are weighting functions for CTDIvol, NPS, and MTF. Specifically, they were defined as

$$D(-d_{ij}, a_d, c_d) = \frac{1}{1+ e^{-a_d(-d_{ij}-c_d)}}, \tag{5}$$

$$T(t_{ij}, a_t, c_t) = \frac{1}{1+e^{-a_t(t_{ij}-c_t)}} - \frac{1}{1+e^{-a_t(t_{ij}+c_t)}}, \tag{6}$$

$$R(r_{ij}, a_r, c_r) = \frac{1}{1+e^{-a_r(r_{ij}-c_r)}} - \frac{1}{1+e^{-a_r(r_{ij}+c_r)}}. \tag{7}$$

The weighting parameters for dose (*D*) and noise texture (*T*) were modified by selecting the parameters that produced visually most comparable image quality between scanners in a prior test (a_d = 10, c_d = 0.5; a_t = 30, c_t = -0.2; a_r = 30, c_r = -0.2). In contrast to the original work, we modified the resolution weighting function *R* to reject kernels with substantially improved spatial resolution (Figure 2) by including a second exponential function in its definition (7).

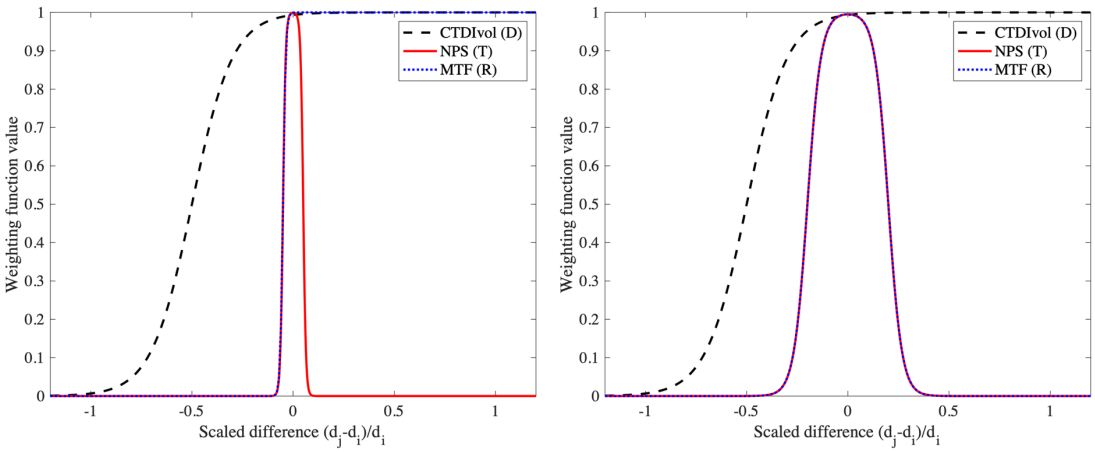

a) Weighting functions from Winslow et al. b) Weighting functions used in this study.

Figure 2. Weighting functions used for finding the optimal reconstruction kernel between CT scanners. a) Weighting functions used in the study by Winslow et al. b) Modified versions of the original weighting functions that were used in this study.

2.4. Tool for image quality harmonization

In this work, an extensive dataset containing a large number of reconstructions (*N* = 5899) was collected. Therefore, the results are mainly presented for one imaging setting (CTDIvol = 10 mGy, 1 mm slice thickness) in the publication. However, the matched kernels for the remaining scan parameters can be found as supplementary material. Furthermore, a dedicated MATLAB (v. 9.2, The MathWorks Inc., Natick, MA, 2017) software and its compiled stand-alone executable versions for Windows and macOS, allowing the reader to perform image quality harmonization with each imaging setting, can be found from (source code: https://github.com/mjuntu/CTHarmonizer;

data, and compiled stand-alone versions: https://doi.org/10.5281/zenodo.5112674). This tool is published under the Creative Commons Attribution 4.0 International license, and it provides software for identifying and visualizing the matching kernels between different scanners.

3. RESULTS

The image quality matching scheme weights the nNPS and MTF equally, thus identifying the kernel that produces a balanced trade-off in image noise and sharpness (Figure 3).

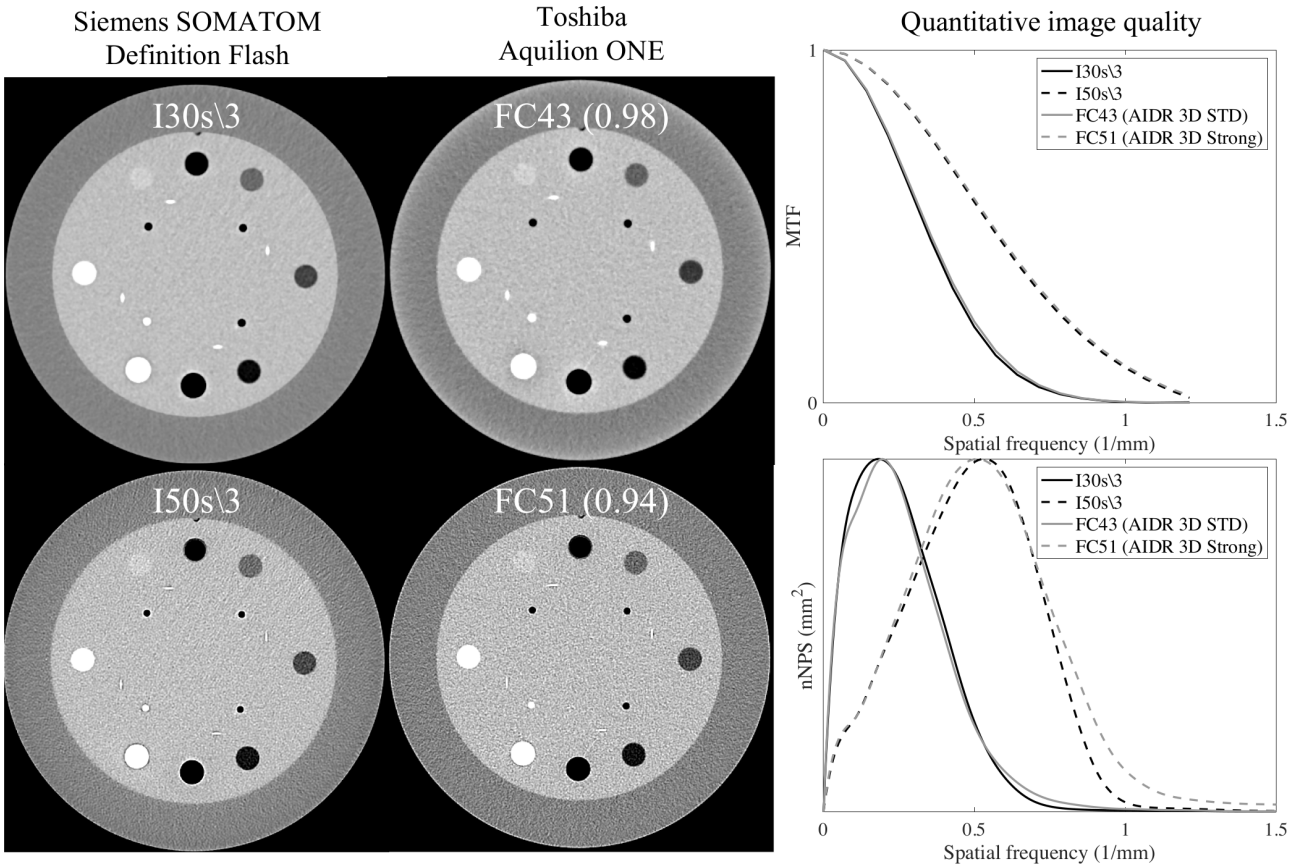

Figure 3. Example reconstructions for Siemens SOMATOM Definition Flash and the corresponding best-matching reconstructions for Toshiba Aquilion One and their MTFs and normalized NPSs (nNPSs) (m-values are indicated in the parentheses, with higher m-value indicating improved agreement). The CTDIvol and slice thickness were 10 mGy and 1 mm, respectively. STD = Standard AIDR 3D strength.

The agreement in image quality, *i.e.,* comparable noise graininess and image sharpness, between the matched reconstruction was generally good (Figure 4). Yet, at sharper kernels, such as the B50s and I50s\3, poorer matches were more frequently observed visually (Figures 4-5). This phenomenon was further evident in the quantitative assessment of the m-values, in which lower values were more frequently observed with sharper reconstruction kernels (Table II).

Interestingly, in some cases, the matched kernel changed when comparing 10 mGy and 40 mGy scans (Figure 5). The tables containing the matched kernels for the remaining scan settings (CTDIvol 10 mGy, 5 mm slice thickness; CTDIvol 40 mGy, 1 mm slice thickness; CTDIvol 40 mGy, 5 mm slice thickness) demonstrate this effect further (see Appendix A). The mean ± standard deviation (median) m-values for the different acquisition settings were: CTDIvol

10 mGy, 1 mm slice: 0.78 ± 0.31 (0.94); CTDIvol 10 mGy, 5 mm slice: 0.75 ± 0.33 (0.93); CTDIvol 40 mGy, 1 mm slice: 0.81 ± 0.28 (0.95); CTDIvol 40 mGy, 5 mm slice: 0.75 ± 0.33 (0.93). The mean ± standard deviation (median) m-values for each scan and reconstruction setting were 0.77 ± 0.31 (0.94).

Distinguishing the noise texture between the to-be-matched reconstruction and the matched reconstruction was difficult with high m-values (m-value > 0.7) (Figure 5). In contrast, with lower m-values (m-value < 0.7), apparent differences in noise graininess were observed (Figure 5), demonstrating consistency between the m-value and visual agreement in image quality.

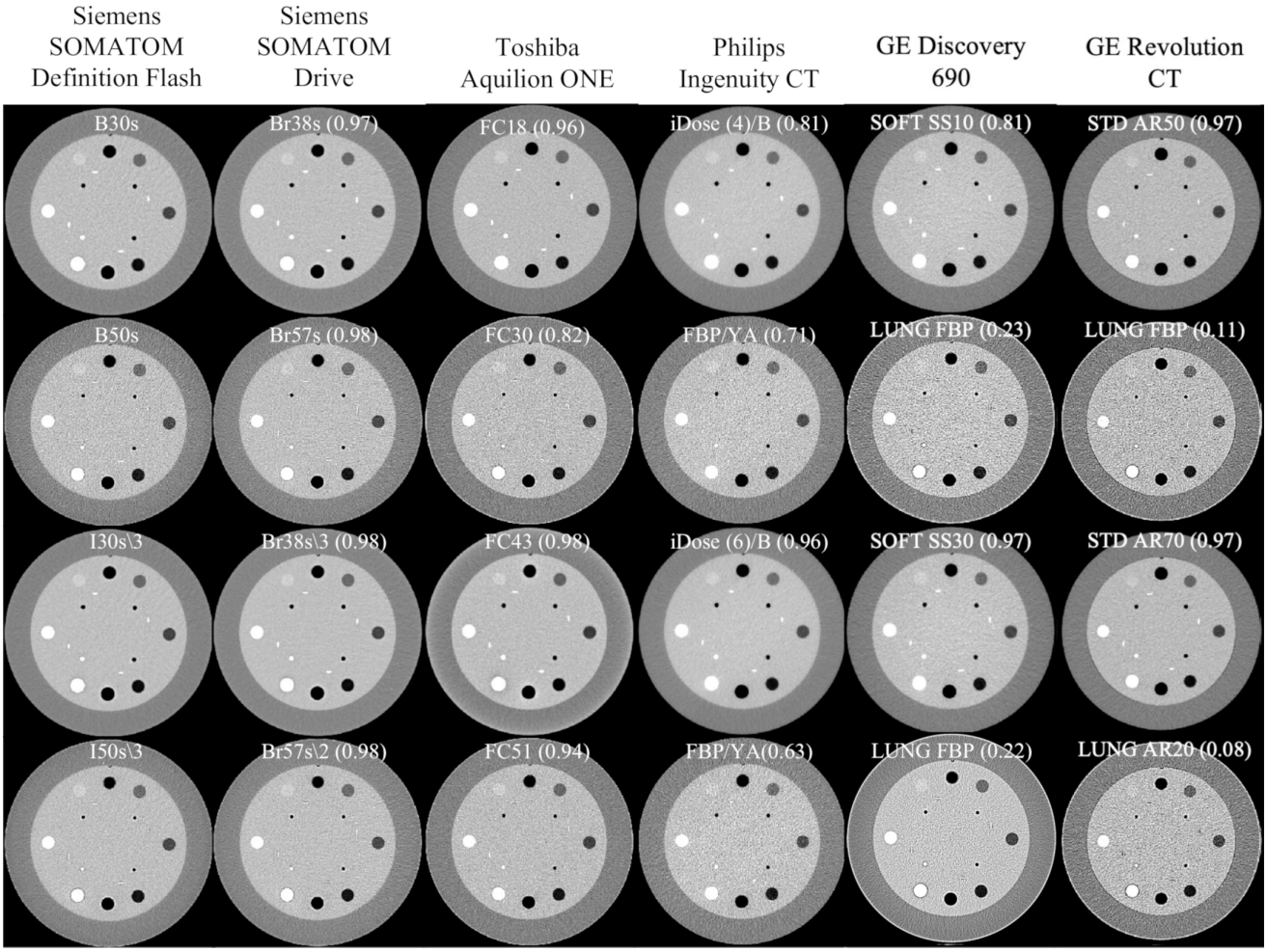

Figure 4. Example reconstructions for Siemens SOMATOM Definition Flash and the corresponding matching reconstructions for the other scanners. The number in the parentheses indicates the matching function value (m-value), for which a higher value indicates better agreement between the reconstructions. The CTDIvol and slice thickness were 10 mGy and 1 mm, respectively. Windowing was set to [-200 HU, 200 HU].

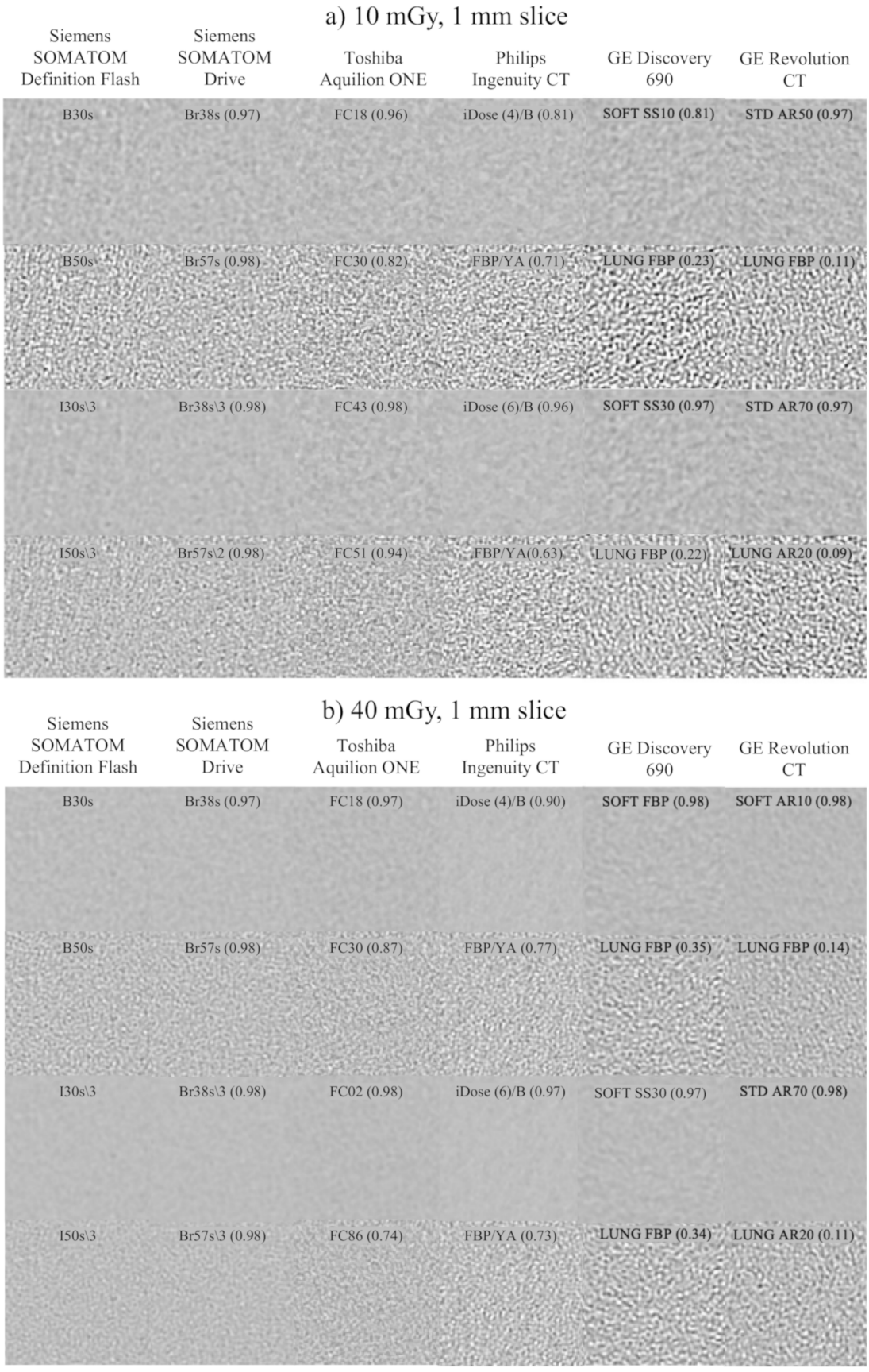

Figure 5. Noise realizations for matched reconstruction kernels for 10 mGy and 40 mGy acquisitions. a) 10 mGy acquisition with 1 mm slice thickness. b) 40 mGy measurement with 1 mm slice thickness. Each row represents one selected kernel for Siemens SOMATOM Definition Flash and the corresponding matched kernels for the other scanners. The number in the parentheses indicates the matching function value (m-value), for which a higher value indicates better agreement between the reconstructions. Windowing was set to [-200 HU, 200 HU].

Table II. Reconstruction kernels for Siemens SOMATOM Definition Flash and the corresponding matched kernels with other scanners for CTDIvol 10 mGy and 1 mm slice. The m-values are presented in the parentheses.

m-value grayscale colorbar

0	0.1	0.2	0.3	0.4	0.5	0.6	0.7	0.8	0.9	1

Flash	Drive	Toshiba	Philips	GE Discovery	GE Revolution
B10s	Br32s (0.98)	FC41 (AIDR 3D STR) (0.93)	iDose (6)/A (0.52)	SOFT_SS90:Slice (0.02)	SOFT#_AR90 (0.87)
B20s	Br34s (0.98)	FC17 (AIDR 3D STD) (0.97)	iDose (1)/A (0.95)	SOFT_SS60:Slice (0.24)	SOFT_AR60 (0.97)
B26s	Br36s\4 (0.98)	FC07 (AIDR 3D eSTD) (0.97)	iDose (4)/A (0.91)	SOFT_SS60:Slice (0.98)	STANDARD_AR90 (0.95)
B30s	Br38s (0.97)	FC18 (AIDR 3D MILD) (0.96)	iDose (4)/B (0.81)	SOFT_SS10:Slice (0.81)	STANDARD_AR50 (0.97)
B31s	Bf37s (0.94)	FC48 (AIDR 3D MILD) (0.94)	FBP/B (0.96)	SOFT_FBP (0.66)	STANDARD_AR20 (0.96)
B35s	Br40s (0.97)	FC26 (AIDR 3D MILD) (0.98)	FBP/B (0.95)	SOFT_FBP (0.92)	STANDARD_AR30 (0.97)
B36s	Bv41s (0.98)	FC64 (AIDR 3D eSTD) (0.95)	FBP/IMR2.Soft Tissue (0.75)	DETAIL_SS50:Slice (0.98)	STANDARD_DLIR_HIGH (0.6)
B40s	Bf37s (0.96)	FC48 (AIDR 3D MILD) (0.95)	FBP/B (0.95)	SOFT_FBP (0.72)	STANDARD_AR30 (0.93)
B41s	Bf42s (0.9)	FC15 (AIDR 3D MILD) (0.91)	FBP/C (0.97)	CHST_FBP (0.74)	CHST_AR30 (0.95)
B45s	Sh49s (0.97)	FC55 (AIDR 3D STR) (0.94)	FBP/C (0.15)	LUNG_SS90:Slice (0.88)	LUNG_AR90 (0.6)
B46s	Bv49s (0.98)	FC50 (AIDR 3D STR) (0.97)	FBP/IMR1.Soft Tissue (0.38)	DETAIL_FBP (0.84)	LUNG_AR80 (0.6)
B50s	Br57s (0.98)	FC30 (AIDR 3D STD) (0.82)	FBP/YA (0.71)	LUNG_FBP (0.23)	LUNG_FBP (0.11)
B60s	Br60s (0.95)	FC31 (AIDR 3D STR) (0.67)	FBP/YA (0.52)	BONEPLUS_SS50:Slice (0.03)	ULTRA_FBP (0.01)
B70s	Br62s (0.98)	FC51 (ORG) (0.88)	FBP/IMR1.SharpPlus (0.86)	BONEPLUS_SS20:Slice (0.53)	BONEPLUS_AR20 (0.57)
B75h	Bv66h\3 (0.95)	FC90 (ORG) (0.96)	iDose (7)/YB (0)	BONE_FBP (0.05)	BONEPLUS_AR100 (0.01)
B80s	Bl57s (0.98)	FC56 (ORG) (0.58)	FBP/YA (0)	LUNG_SS10:Slice (0.94)	LUNG_FBP (0.97)
I26s\1	Br38s (0.98)	FC19 (AIDR 3D STR) (0.98)	iDose (5)/B (0.92)	SOFT_SS10:Slice (0.95)	STANDARD_AR60 (0.97)
I26s\2	Br38s\2 (0.98)	FC42 (AIDR 3D MILD) (0.98)	iDose (5)/B (0.95)	SOFT_SS20:Slice (0.97)	STANDARD_AR70 (0.97)
I26s\3	Br38s\3 (0.98)	FC43 (AIDR 3D STD) (0.98)	iDose (6)/B (0.96)	SOFT_SS30:Slice (0.97)	STANDARD_AR70 (0.97)
I26s\4	Br38s\4 (0.98)	FC02 (AIDR 3D STD) (0.97)	iDose (6)/B (0.96)	SOFT_SS40:Slice (0.97)	DETAIL_AR100 (0.97)
I26s\5	Br38s\5 (0.98)	FC01 (AIDR 3D eSTD) (0.96)	iDose (6)/B (0.84)	SOFT_SS50:Slice (0.96)	DETAIL_AR100 (0.97)
I30s\1	Br38s (0.98)	FC19 (AIDR 3D STR) (0.98)	iDose (5)/B (0.91)	SOFT_SS10:Slice (0.94)	STANDARD_AR60 (0.97)
I30s\2	Hc40s (0.98)	FC42 (AIDR 3D MILD) (0.98)	iDose (5)/B (0.94)	SOFT_SS20:Slice (0.96)	STANDARD_AR70 (0.97)
I30s\3	Br38s\3 (0.98)	FC43 (AIDR 3D STD) (0.98)	iDose (6)/B (0.96)	SOFT_SS30:Slice (0.97)	STANDARD_AR70 (0.97)
I30s\4	Bv38s\3 (0.97)	FC70 (AIDR 3D STR) (0.97)	iDose (6)/B (0.94)	SOFT_SS50:Slice (0.96)	DETAIL_AR100 (0.96)

I30s\5	Br36s\5 (0.97)	FC22 (AIDR 3D STD) (0.96)	iDose (6)/A (0.79)	SOFT_SS70:Slice (0.93)	STANDARD_AR100 (0.9)
I31s\1	Bf37s (0.98)	FC48 (AIDR 3D MILD) (0.98)	FBP/B (0.98)	STANDARD_FBP (0.85)	CHST_AR70 (0.97)
I31s\2	Bf39s (0.97)	FC21 (ORG) (0.98)	FBP/B (0.98)	STANDARD_SS10:Slice (0.89)	CHST_AR70 (0.97)
I31s\3	Bf37s\2 (0.96)	FC02 (ORG) (0.97)	iDose (2)/B (0.97)	STANDARD_SS30:Slice (0.89)	CHST_AR80 (0.97)
I31s\4	Bf37s\4 (0.96)	FC12 (AIDR 3D eSTD) (0.97)	iDose (5)/B (0.96)	CHST_SS60:Slice (0.9)	DETAIL_AR80 (0.96)
I31s\5	Qv43s (0.97)	FC22 (AIDR 3D MILD) (0.91)	iDose (6)/B (0.87)	CHST_SS90:Slice (0.8)	DETAIL_AR100 (0.9)
I36s\1	Hr49s (0.98)	FC49 (ORG) (0.9)	FBP/IMR1.Soft Tissue (0.93)	DETAIL_FBP (0.97)	CHST_AR50 (0.56)
I36s\2	Hr49s\1 (0.97)	FC83 (AIDR 3D STR) (0.95)	FBP/IMR1.Soft Tissue (0.95)	DETAIL_FBP (0.98)	CHST_AR50 (0.38)
I36s\3	Hr49s\3 (0.97)	FC49 (AIDR 3D eSTD) (0.97)	FBP/IMR1.Soft Tissue (0.93)	DETAIL_SS10:Slice (0.96)	STANDARD_DLIR_LOW (0.29)
I36s\4	Hr49s\4 (0.94)	FC24 (AIDR 3D eSTD) (0.95)	FBP/IMR1.Soft Tissue (0.8)	DETAIL_SS20:Slice (0.93)	STANDARD_DLIR_MEDIUM (0.28)
I36s\5	Hr49s\5 (0.89)	FC70 (AIDR 3D eSTD) (0.94)	FBP/IMR2.Soft Tissue (0.63)	DETAIL_SS40:Slice (0.82)	STANDARD_DLIR_HIGH (0.16)
I40s\1	Hc44s (0.98)	FC48 (AIDR 3D MILD) (0.98)	FBP/B (0.97)	STANDARD_FBP (0.92)	CHST_AR70 (0.95)
I40s\2	Hc44s\1 (0.98)	FC48 (AIDR 3D MILD) (0.98)	FBP/B (0.97)	STANDARD_SS10:Slice (0.95)	CHST_AR70 (0.96)
I40s\3	Bf37s\2 (0.98)	FC21 (AIDR 3D eSTD) (0.98)	iDose (2)/B (0.97)	STANDARD_SS30:Slice (0.96)	CHST_AR80 (0.97)
I40s\4	Bf37s\4 (0.98)	FC79 (AIDR 3D STR) (0.97)	iDose (5)/B (0.95)	CHST_SS60:Slice (0.96)	CHST_AR90 (0.97)
I40s\5	Qv43s (0.98)	FC02 (AIDR 3D eSTD) (0.95)	iDose (6)/B (0.91)	CHST_SS90:Slice (0.93)	CHST_AR100 (0.95)
I41s\1	Bf42s (0.97)	FC15 (AIDR 3D MILD) (0.94)	iDose (1)/C (0.97)	CHST_FBP (0.92)	CHST_AR50 (0.91)
I41s\2	Bf42s (0.97)	FC14 (ORG) (0.96)	iDose (3)/C (0.97)	CHST_FBP (0.95)	CHST_AR50 (0.9)
I41s\3	Bf42s\2 (0.96)	FC04 (ORG) (0.95)	iDose (4)/C (0.96)	CHST_SS10:Slice (0.95)	CHST_AR60 (0.87)
I41s\4	Bf42s\4 (0.95)	FC23 (AIDR 3D eSTD) (0.97)	iDose (6)/C (0.94)	DETAIL_SS30:Slice (0.91)	STANDARD_DLIR_HIGH (0.76)
I41s\5	Bf42s\5 (0.93)	FC13 (AIDR 3D eSTD) (0.97)	FBP/IMR2.Soft Tissue (0.88)	DETAIL_SS60:Slice (0.79)	CHST_AR90 (0.65)
I44s\1	Hv45s\5 (0.96)	FC05 (AIDR 3D eSTD) (0.97)	FBP/IMR2.Routine (0.48)	DETAIL_SS10:Slice (0.93)	LUNG_AR100 (0.07)
I44s\2	Bv41s\5 (0.89)	FC79 (AIDR 3D eSTD) (0.73)	FBP/IMR2.Routine (0.03)	BONE_SS100:Slice (0.6)	LUNG_AR100 (0.02)
I44s\3	Bv41s\5 (0.63)	FC64 (AIDR 3D eSTD) (0.1)	FBP/IMR2.Soft Tissue (0)	DETAIL_SS40:Slice (0.16)	STANDARD_DLIR_HIGH (0)
I44s\4	Bv41s\5 (0.29)	FC64 (AIDR 3D eSTD) (0.03)	FBP/IMR2.Soft Tissue (0)	DETAIL_SS60:Slice (0.05)	STANDARD_DLIR_HIGH (0)
I44s\5	Bv41s\5 (0.04)	FC62 (AIDR 3D eSTD) (0.03)	FBP/IMR3.Routine (0.01)	DETAIL_SS90:Slice (0.08)	CHST_AR100 (0)
I46s\1	Hv45s (0.98)	FC50 (AIDR 3D STD) (0.94)	FBP/IMR1.Routine (0.73)	DETAIL_FBP (0.48)	LUNG_AR70 (0.43)
I46s\2	Hv45s\2 (0.98)	FC83 (AIDR 3D STD) (0.96)	FBP/IMR1.Routine (0.76)	DETAIL_FBP (0.74)	LUNG_AR80 (0.32)
I46s\3	Bv49s\3 (0.98)	FC83 (AIDR 3D STD) (0.97)	FBP/IMR1.Routine (0.68)	DETAIL_FBP (0.9)	LUNG_AR80 (0.16)
I46s\4	Hv45s\4 (0.96)	FC05 (AIDR 3D eSTD) (0.93)	FBP/IMR2.Routine (0.85)	DETAIL_FBP (0.94)	LUNG_AR90 (0.05)

I46s\5	Bv49s\5 (0.94)	FC05 (AIDR 3D eSTD) (0.94)	FBP/IMR2.Routine (0.61)	DETAIL_SS20:Slice (0.87)	LUNG_AR100 (0.02)
I49s\1	Sb49s\1 (0.97)	FC55 (AIDR 3D eSTD) (0.96)	FBP/C (0.75)	LUNG_SS90:Slice (0.89)	LUNG_AR100 (0.9)
I49s\2	Sb49s\2 (0.97)	FC48 (ORG) (0.96)	iDose (1)/C (0.86)	CHST_FBP (0.93)	LUNG_AR100 (0.87)
I49s\3	Sh49s\3 (0.97)	FC48 (ORG) (0.96)	iDose (5)/C (0.91)	STANDARD_FBP (0.98)	STANDARD_DLIR_LOW (0.93)
I49s\4	Qv43s\5 (0.97)	FC64 (ORG) (0.97)	iDose (6)/C (0.83)	CHST_SS50:Slice (0.98)	STANDARD_DLIR_HIGH (0.9)
I49s\5	Bv40s\5 (0.97)	FC62 (AIDR 3D eSTD) (0.9)	FBP/IMR3.Routine (0.59)	STANDARD_SS90:Slice (0.96)	CHST_AR100 (0.8)
I50s\1	Br57s (0.98)	FC30 (AIDR 3D STD) (0.92)	FBP/YA (0.71)	LUNG_FBP (0.24)	LUNG_FBP (0.09)
I50s\2	Br57s\1 (0.98)	FC30 (AIDR 3D STD) (0.94)	FBP/YA (0.7)	LUNG_FBP (0.24)	LUNG_AR10 (0.09)
I50s\3	Br57s\2 (0.98)	FC51 (AIDR 3D STR) (0.94)	FBP/YA (0.63)	LUNG_FBP (0.22)	LUNG_AR20 (0.08)
I50s\4	Br57s\4 (0.96)	FC86 (AIDR 3D STR) (0.91)	FBP/IMR1.Routine (0.63)	BONEPLUS_SS90:Slice (0.61)	LUNG_AR40 (0.05)
I50s\5	Qr49s\3 (0.82)	FC50 (AIDR 3D eSTD) (0.89)	FBP/IMR1.Routine (0.84)	BONE_SS90:Slice (0.74)	LUNG_AR70 (0.01)
I70h\1	Br62s\2 (0.98)	FC53 (AIDR 3D STR) (0.98)	FBP/IMR2.SharpPlus (0.51)	BONEPLUS_SS30:Slice (0.42)	BONEPLUS_AR50 (0.3)
I70h\2	Br62s\3 (0.97)	FC52 (AIDR 3D MILD) (0.98)	FBP/IMR2.SharpPlus (0.32)	BONEPLUS_SS40:Slice (0.44)	BONEPLUS_AR60 (0.24)
I70h\3	Br62s\4 (0.95)	FC52 (AIDR 3D MILD) (0.97)	FBP/IMR2.SharpPlus (0.15)	BONEPLUS_SS40:Slice (0.48)	BONEPLUS_AR70 (0.16)
I70h\4	Br62s\4 (0.89)	FC31 (AIDR 3D eSTD) (0.94)	iDose (7)/YA (0.12)	BONEPLUS_SS60:Slice (0.68)	BONEPLUS_AR90 (0.05)
I70h\5	Br62s\5 (0.92)	FC52 (AIDR 3D eSTD) (0.96)	iDose (7)/YA (0.13)	BONEPLUS_SS70:Slice (0.91)	BONEPLUS_AR100 (0.01)

DLIR = Deep learning image reconstruction eSTD = Enhanced standard, ORG = original filtered back projection, STD = Standard, STR = Strong.

4. DISCUSSION

This study followed the work by Winslow et al for matching technical image quality between different CT scanners (Winslow *et al* 2017). The method by Winslow et al was modified and extended for additional CT scanners, vendors, and reconstruction algorithms. Overall, the matching technique provided visually comparable reconstruction pairs between different CT scanners for the Catphan phantom. In some of the presented reconstructions, visually observable differences were evident, but in these cases, the poorer match was typically indicated by a lower m-value (m-value < 0.7). Consequently, the matching scheme provided relevant feedback for the user on its confidence in the matching. For a reconstruction pair with a visually poor agreement, the low m-value indicates that there was no comparable reconstruction with similar noise coarseness and image sharpness.

In general, weaker matches were found with sharper kernels. Similarly, Solomon et al. demonstrated that the higher frequency kernels for Siemens (B50f, B60f, B70f, B80f) generally exhibited poorer agreement in NPS between the matched GE kernels when compared to softer and medium-coarse kernels (B20f – B46f) (Solomon *et al* 2012). In addition, previous research also demonstrates low matching function values (m-value < 10^{-5}) between the I44s kernel of Somatom Definition Flash and those of GE Discovery CT 750HD 120 (Winslow *et al* 2017). This particular kernel provides a very sharp image while simultaneously regularizing noise strongly, and no comparable kernel was found for other scanners.

Despite the aforementioned agreements between these results and those from previous research, specific modifications to the weighting functions were made compared to the original study (Winslow *et al* 2017). In several cases with the same peak frequency for the NPS, the shape of the NPS curves deviated substantially between reconstruction kernels and algorithms. Although the peak NPS frequency difference provides an intuitive, and in many cases, visually acceptable description of the noise texture, particularly for FBP (Solomon *et al* 2012), the shape of the NPS may deviate substantially between FBP and IR (Geyer *et al* 2015, Ghetti *et al* 2013). Consequently, the RMSE was considered a more robust method for identifying the closest matching noise texture. Regarding the comparison of MTF, an RMSE based approach was also adopted since using the spatial frequency at which the MTF is decreased by 50% solely may lose information related to edge sharpening (Winslow *et al* 2017). Furthermore, in contrast to the work by Winslow et al, a substantially improved spatial resolution was not allowed, and the difference in MTF was weighted with a bell-shaped curve rather than a high-pass-type logistic function. This change was implemented because if the image quality of the to-be-matched imaging protocol and reconstruction kernel is

optimized for a specific task, a further improvement in MTF would not necessarily be needed. In such a situation, the radiation dose could be reduced instead, for example. This may be the case when harmonizing image quality between an older and a newer scanner with more dose-efficient scans. However, as discussed in a previous study (Winslow *et al* 2017), the optimization strategy and thus the weighting function naturally varies between organizations.

Specific limitations need to be addressed. First, to limit the amount of data, the reconstructions were collected only for body region kernels, and the head kernels were excluded. However, the matching technique also works for head kernels, and the kernel matching software, included as a supplementary document, can be used for both body and head kernels. Second, the matching paradigm only considers technical measures for image quality. This approach was selected since MTF and NPS are commonly used, quantitative, and intuitive measures for medical physicists. However, IR algorithms have been shown to exhibit non-linear behavior in noise properties with respect to anatomical texture (Solomon and Samei 2014) and resolution with respect to imaging task and radiation dose (Richard *et al* 2012), which should be considered in the future development of the method. An alternative approach would be to use subjective image quality metrics (model observers) to approximate the visual assessment by human observers (Verdun *et al* 2015, Barrett *et al* 1993, Christianson *et al* 2015).

In the present study, only one set of weighting parameters was used for the matching technique. In practice, however, the diagnostic task should be considered when selecting the optimal weighting parameters (Richard *et al* 2012, Samei *et al* 2014). For illustration, for volume quantification tasks, such as coronary artery calcium scoring, the preservation of spatial resolution is crucial (Juntunen *et al* 2021), and consequently, the MTF could be weighted more than the NPS during the matching. In contrast, applications requiring excellent low contrast detectability, such as tumor diagnostics, may benefit from a weighting that prioritizes agreement in NPS. Consequently, the matching scheme may benefit from task-based modifications to the weights (Chen *et al* 2014, Richard *et al* 2012). The source code for the supplemented software is shared, and the user may freely modify the weighting functions based on their organization's needs.

5. CONCLUSION

This study demonstrated the utility of combined quantitative assessment of NPS and MTF in harmonizing the technical image quality between CT scanners, vendors, and institutions. Software, developed for this purpose and

containing the data for image quality harmonization, was also shared to support others aiming to harmonize the image quality in their institutions. As future work, since IR has been shown to exhibit tissue-dependent changes in noise texture (Solomon and Samei 2014), the noise properties could be directly determined from different tissues (Solomon and Samei 2013, 2014, Vegas-Sánchez-Ferrero *et al* 2019). Such a method may allow for an even more diagnostically grounded approach for harmonization of image quality.

REFERENCES

Angel E 2012 AIDR 3D Iterative Reconstruction: Integrated, Automated and Adaptive Dose Reduction *White Pap.* 1–10

Barrett H H, Yao J, Rolland J P and Myers K J 1993 Model observers for assessment of image quality *Proc. Natl. Acad. Sci. U. S. A.* **90** 9758–65

Boedeker K L, Cooper V N and McNitt-Gray M F 2007 Application of the noise power spectrum in modern diagnostic MDCT: part I. Measurement of noise power spectra and noise equivalent quanta *Phys. Med. Biol.* **52** 4027–46 Online: https://iopscience.iop.org/article/10.1088/0031-9155/52/14/002

Boedeker K L and McNitt-Gray M F 2007 Application of the noise power spectrum in modern diagnostic MDCT: part II. Noise power spectra and signal to noise *Phys. Med. Biol.* **52** 4047–61 Online: https://iopscience.iop.org/article/10.1088/0031-9155/52/14/003

Chen B, Ramirez Giraldo J C, Solomon J and Samei E 2014 Evaluating iterative reconstruction performance in computed tomography *Med. Phys.* **41** 121913 Online: http://doi.wiley.com/10.1118/1.4901670

Christianson O, Chen J J S, Yang Z, Saiprasad G, Dima A, Filliben J J, Peskin A, Trimble C, Siegel E L and Samei E 2015 An Improved Index of Image Quality for Task-based Performance of CT Iterative Reconstruction across Three Commercial Implementations *Radiology* **275** 725–34 Online: http://pubs.rsna.org/doi/10.1148/radiol.15132091

Fan J, Yue M and Melnyk R 2014 *Whitepaper: GE Healthcare Benefits of ASiR-V * Reconstruction for Reducing Patient Radiation Dose and Preserving Diagnostic Quality in CT Exams* Online: https://onedrive.live.com/?authkey=%21ACcu-zRYgh0d4RY&cid=AA4F6A81A8702730&id=AA4F6A81A8702730%21353473&parId=AA4F6A81A8702730%21348176&o=OneUp

Geyer L L, Schoepf U J, Meinel F G, Nance J W, Bastarrika G, Leipsic J A, Paul N S, Rengo M, Laghi A and De Cecco C N 2015 State of the Art: Iterative CT reconstruction techniques[1] *Radiology* **276** 339–57

Ghetti C, Palleri F, Serreli G, Ortenzia O and Ruffini L 2013 Physical characterization of a new CT iterative reconstruction method operating in sinogram space *J. Appl. Clin. Med. Phys.* **14** 263–71 Online: http://doi.wiley.com/10.1120/jacmp.v14i4.4347

Grant K and Raupach R 2012 *SAFIRE: Sinogram Affirmed Iterative Reconstruction* Online: www.usa.siemens.com/healthcare

Hernandez-Giron I, Veldkamp W J H and Geleijns J 2018 AIDR 3D Enhanced — The latest hybrid model-based iterative dose reduction technology from Canon *White Pap.*

Hou Y, Liu X, Xv S, Guo W and Guo Q 2012 Comparisons of image quality and radiation dose between iterative reconstruction and filtered back projection reconstruction algorithms in 256-MDCT coronary angiography *Am. J. Roentgenol.* **199** 588–94

Hsieh J, Liu E, Nett B, Tang J, Thibault J-B and Sahney S 2019 A new era of image reconstruction: TrueFidelity™ Technical white paper on deep learning image reconstruction Online: https://www.gehealthcare.com/products/truefidelity

Juntunen M A K, Kotiaho A O, Nieminen M T and Inkinen S I 2021 Optimizing iterative reconstruction for quantification of calcium hydroxyapatite with photon counting flat-detector computed tomography: a cardiac phantom study *J. Med. Imaging* **8** Online: https://www.spiedigitallibrary.org/journals/journal-of-medical-imaging/volume-8/issue-05/052102/Optimizing-iterative-reconstruction-for-quantification-of-calcium-hydroxyapatite-with-photon/10.1117/1.JMI.8.5.052102.full

Mehta D, Thompson R, Morton T, Dhanantwari E, Shefer E, Dhanantwari A, Shefer E and Healthcare P 2013 Iterative model reconstruction: simultaneously lowered computed tomography radiation dose and improved image quality *Med. Phys. Int.* **1** 147–55

Ramirez-Giraldo J C, Grant K L and Raupach R 2014 *Whitepaper: Advanced Modeled Iterative*

Reconstruction

Richard S, Husarik D B, Yadava G, Murphy S N and Samei E 2012 Towards task-based assessment of CT performance: System and object MTF across different reconstruction algorithms *Med. Phys.* **39** 4115–22 Online: http://doi.wiley.com/10.1118/1.4725171

Samei E, Richard S and Lurwitz L 2014 Model-based CT performance assessment and optimization for iodinated and noniodinated imaging tasks as a function of kVp and body size *Med. Phys.* **41** 081910 Online: http://doi.wiley.com/10.1118/1.4890082

Solomon J B, Christianson O and Samei E 2012 Quantitative comparison of noise texture across CT scanners from different manufacturers *Med. Phys.* **39** 6048–55 Online: http://doi.wiley.com/10.1118/1.4752209

Solomon J and Samei E 2013 Are uniform phantoms sufficient to characterize the performance of iterative reconstruction in CT? *Medical Imaging 2013: Physics of Medical Imaging*

Solomon J and Samei E 2014 Quantum noise properties of CT images with anatomical textured backgrounds across reconstruction algorithms: FBP and SAFIRE *Med. Phys.* **41**

Vegas-Sánchez-Ferrero G, Ledesma-Carbayo M J, Washko G R and San José Estépar R 2019 Harmonization of chest CT scans for different doses and reconstruction methods *Med. Phys.* **46** 3117–32 Online: https://onlinelibrary.wiley.com/doi/10.1002/mp.13578

Verdun F R, Racine D, Ott J G, Tapiovaara M J, Toroi P, Bochud F O, Veldkamp W J H, Schegerer A, Bouwman R W, Giron I H, Marshall N W and Edyvean S 2015 Image quality in CT: From physical measurements to model observers *Phys. Medica* **31** 823–43 Online: http://dx.doi.org/10.1016/j.ejmp.2015.08.007

Willemink M J, De Jong P A, Leiner T, De Heer L M, Nievelstein R A J, Budde R P J and Schilham A M R 2013 Iterative reconstruction techniques for computed tomography Part 1 : Technical principles Iterative Reconstruction in Image Space *Eur. Radiol.* **23** 1623–31 Online: http://link.springer.com/10.1007/s00330-012-2765-y

Winslow J, Zhang Y and Samei E 2017 A method for characterizing and matching CT image quality across CT scanners from different manufacturers *Med. Phys.* **44** 5705–17 Online: http://doi.wiley.com/10.1002/mp.12554